

Oil Inclusions Found in Skeleton Crystals of Quartz Indicated the Existence of Organic Matter Surrounding Ancient Growth Environments

Yuki Sugiura,* Naoko Tobita, Takashi Tobita, Masaru Taga, Shu Nakachi, Kazumichi Yokota, Etsuko Yamada, Masanori Horie, Koichi Momma, and Satoshi Matsubara



Cite This: *ACS Omega* 2023, 8, 21464–21473



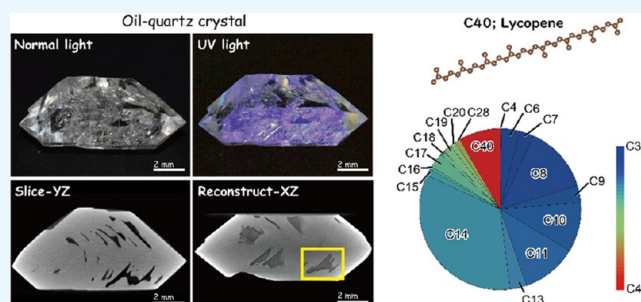
Read Online

ACCESS |

Metrics & More

Article Recommendations

ABSTRACT: In nature, minerals record various origins and information for geology and geobiochemistry. Here, we investigated the origin of organic matter and growth mechanism of quartz with oil inclusion revealing fluorescence under short ultraviolet (UV) light, obtained from the clay vein at Shimantocho, Kochi, Shikoku Island, Japan. Geological investigation indicated that the oil–quartz was formed in hydrothermal metamorphic veins found in the late Cretaceous interbedded sandstone and mudstone. The obtained oil–quartz crystals are mostly double-terminated. Micro-X-ray computed tomography (microCT) indicated that oil–quartz crystals have various veins originating as skeleton structures along the quartz crystal $\{111\}$ and $\{1-11\}$ faces. Spectroscopic and chromatographic studies indicated that aromatic ester and tetraterpene (lycopene) molecules, which revealed fluorescence, were detected. Large molecular weight sterol molecules, such as C40, were also detected in the vein of oil–quartz. This investigation indicated that organic inclusions in mineral crystals would form with ancient microorganism culture environments.



1. INTRODUCTION

Unlike in industrial processes and laboratory materials, almost all natural minerals contain various solid–liquid–gas phases as inclusions and additives.^{1–3} These inclusions are occasionally regarded as unnecessary objects, but they also play precious roles for such minerals like the star effect for sapphire, phantom quartz, and alexandrite.^{4–7} The inclusions have recorded the conditions and processes of the geological formation and become the key to the discovery for new materials such as lasers, optical devices, semiconductors, and electronics for sustainable chemistry and natural resources.

Organic material-related structures in various scales of geological settings have attracted attention for not only mineralogy, geology, and geochemistry but also materials sciences, bioceramics, medical equipment, and green chemistry. The silica clathrate compound and layered materials, typified zeolite and mica, were already widely applied as ionic exchange materials and biomedical materials because of their biocompatibility and low environmental loading.^{8–11} Moreover, recently, organic molecule substitution and hybridization to silica-based minerals found in various geological scales have attracted attention for new aspects of mineralogy, igneous petrology, and astrobiology for chemical evolution, origin of life, and electrocatalytic effects,^{12–15} for example, “Hayabusa2 artificial satellite project.” The relationships of organic

molecules and inorganic minerals were considered the key to the origin of life and Earth.¹⁶

Previous studies have reported that the typical silicate mineral quartz (SiO_2) was sometimes found with organic matters in its crystals as negative crystals and/or surface coating.^{17–20} Suchy et al.²¹ discussed the formation sequences of organic inclusions in quartz obtained from the west region of the Czech Republic, analyzing by mass spectroscopic methods. However, the relationships between the states of organic inclusions in quartz and surrounding rocks were still unclear.

In this study, we focused on fluorescence quartz (oil–quartz) found from a sedimentary rock of southwest region, Shikoku Island, Southwest, Japan. Results showed that the origin of fluorescence regions in oil–quartz is attributed to its geological setting.

Received: January 14, 2023

Accepted: May 18, 2023

Published: June 5, 2023



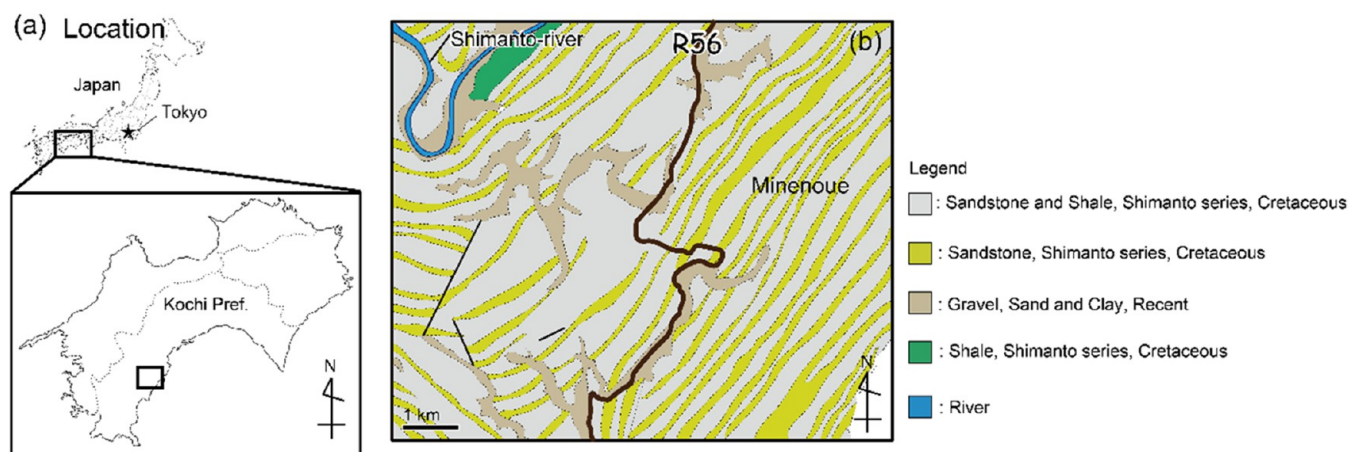


Figure 1. (a) Location of Shimanto area, Kochi prefecture, Shikoku Island, Japan. (b) Geological mapping of the survey area in this study. Modified from the geological map Kubokawa, Geological Survey of Japan, 1933²³ with reprint permitted.

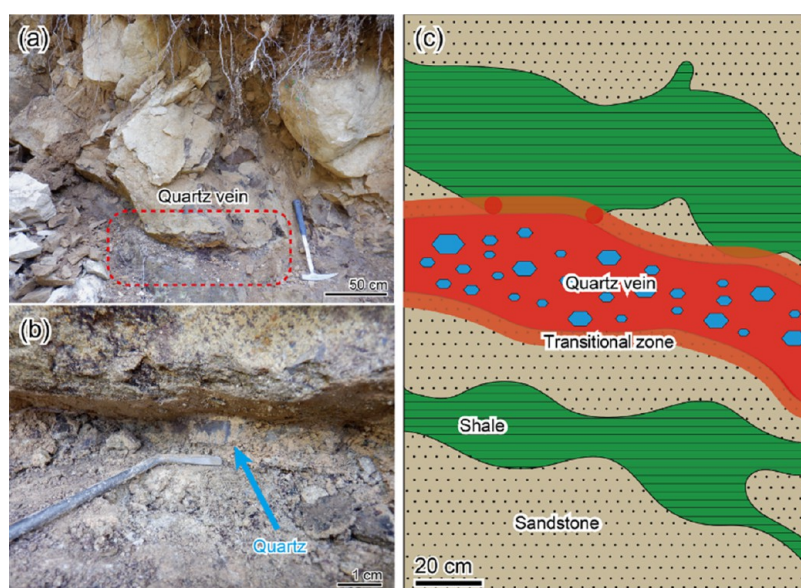


Figure 2. (a) Photograph of the outcrop of quartz veins obtained from oil–quartz crystals. (b) Photograph of the quartz veins and paragenesis of oil–quartz crystals in veins. (c) Schematic image of the structure of quartz veins and paragenesis of oil–quartz crystals.

2. RESULTS AND DISCUSSION

2.1. Geological Setting: Regional Geology. The regional stratigraphy and geology of the study area, Shimanto region, have been summarized by Katto et al.²² The collection site is located in the Nonogawa formation, Shimanto supergroup, developed at the southwest region of Shikoku Island, Japan (Figure 1a).^{23–25} The Shimanto belt was categorized as a typical accretionary prism at the subduction zone of the Philippine Sea Plate sneaking into the Eurasian Plate. Radiolarian age analysis indicated that the sedimentary age of the Nonogawa formation was later Santonian to former Campanian of the Cretaceous period.²⁶ The Nonogawa formation primarily comprised alternate sandstone and shale layers of 10 m thickness with small amounts of chert and acidic tuff (Figure 1b).²⁷

The lens-like clay veins probably formed via hydrothermal alteration are observed in the interbedded sandstone and shale. The width of the lens-like clay veins varies from several cm to m in thickness (Figure 2a). Oil–quartz crystals were found in the clay veins (Figure 2b). All rock and quartz samples were

obtained from an outcrop of a stratum located at Minehou, Shimanto-cho, Kochi prefecture, Japan; 33.169029 north, 133.139936 east. All obtained rock samples for further evaluations were trimmed to remove the surface-weathered part.

2.2. Occurrence of Oil–Quartz Paragenesis and Surrounding Rock Conditions. The quartz crystals were obtained from yellowish colored clay veins with sandstone. Most quartz crystals were double-terminated, and the direction of the *c*-axis is parallel to the strike of clay veins. Sometimes, the parallel intergrowth of quartz crystals was observed. The length of the *c*-direction varies from several cm to 10 cm.

The color of the adjacent sandstone was a bit dark compared to that of the normal sandstone in the outcrop. In this study, therefore, we divided rock samples into three parts based on the relationships of quartz veins: mother rock, transition zone, and clay vein (Figure 2c).

Figure 3 shows the thin sections of each zone of rock core samples. In the cases of the parent rock and transition zone, a bit rounded colored minerals and colorless minerals identified

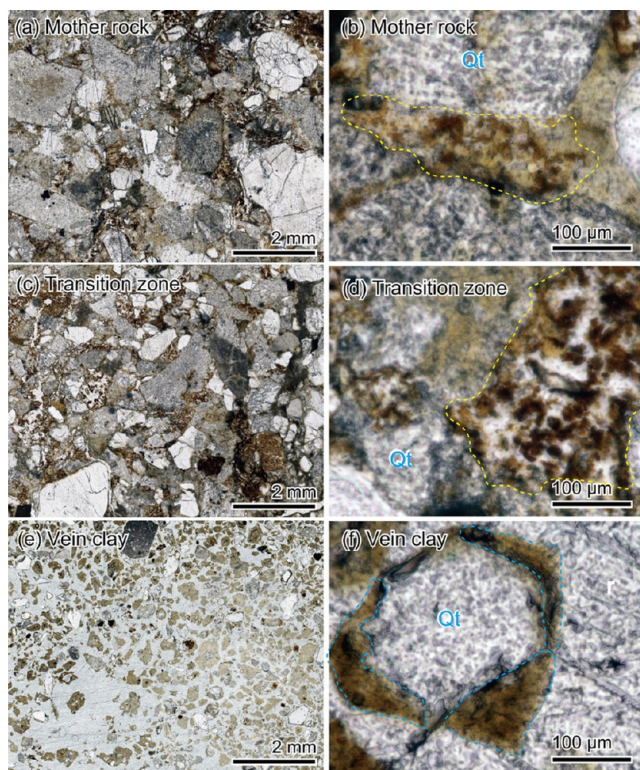


Figure 3. Thin section of the typical structure of rock cores. (a, b) Parent rock. (c, d) Transition zone. (e, f) Vein clay. Qt: quartz. Yellow broken line area: the organic particle-aggregated areas. Blue broken line: the unformed organic particle-aggregated areas.

as quartz and feldspar were commonly observed, respectively. They were approximately several 100 μm in size. Many brownish organic particles around several 10 μm in sizes were also observed in quartz and feldspar crystals. In the case of the transition zone, the distribution and structure of minerals were mostly the same as those of the parent rocks, but a few chlorite particles were also observed. Meanwhile, in the clay vein, a brownish membrane structure surrounding quartz crystals was observed, instead of brownish organic particles. In addition, few feldspar particles were observed. This tendency of the mineral component in each rocks was estimated by bulk X-ray diffraction (XRD) measurement. Figure 4 shows the X-ray diffraction (XRD) patterns of each zone of rock core samples. Although obviously strong peaks identified as feldspar were detected in the parent rock and transition zone, no significant peaks of feldspar were observed in the clay vein, but several clay minerals such as montmorillonite were identified. The fine structures of clay minerals in the clay vein were observed.

Figure 5 shows the SEM micrographs of the clay vein. The clay vein comprises scaly materials with typical clay minerals and few fiber-like particles around several 100 nm in size.

The bulk compositions of inorganic and organic compounds in each samples were measured. Table 1 shows the bulk compositions of each rock core sample measured via X-ray fluorescence (XRF) spectroscopy. The clay vein contained lower K and higher Al and Fe compositions than those of the parent rock and transition zone, which indicate that the alteration of the hydrothermal solution into the parent rock caused the clay vein formation. In addition, we measured total carbon contents and organic carbon contents of samples. Figure 6 shows the total carbon contents and organic carbon

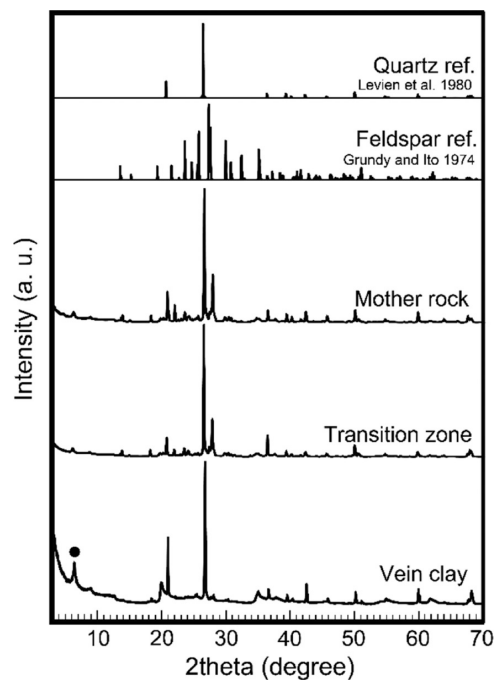


Figure 4. XRD patterns of rock core samples with reference quartz⁴⁹ and feldspar⁵⁰ patterns with {hkl} indexes for facilitating comparison. ●: montmorillonite.⁵¹

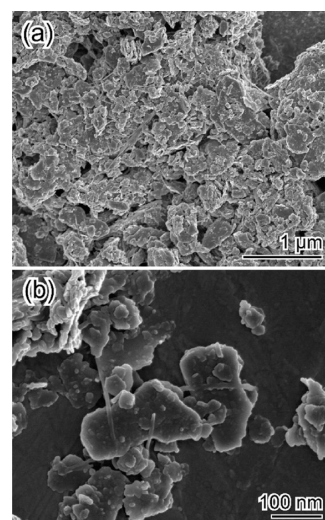


Figure 5. SEM micrographs of the vein clay. (a) Low magnification. (b) High magnification.

contents of samples. The carbon content, particularly the organic carbon content of the clay vein, was approximately 10 times higher than those of the parent rock and transition zone.

2.3. Analysis of the Oil–Quartz Crystal Sample. Figure 7 shows the representative photograph of oil–quartz crystals. They were mostly obtained as double-terminated crystals. Under UV (235 nm) light, blue- and/or orange-colored luminescence domains were observed in oil–quartz crystals. Although the domains around several 10 μm in size (smaller distributions) were particle-like, larger luminescence domains had normally lineal or membranous shapes. In addition, the sizes of lineally or membranous shaped domains were consistent with the sizes of parent quartz crystals. The luminescence domains in the voids of quartz crystals were

Table 1. XRF Analysis Results of Bulk Chemical Compositions of Rock Core Samples^a

atom %	mother rock	transition zone	vein clay
SiO ₂	64.38 ± 0.35	62.16 ± 0.05	56.26 ± 0.30
Al ₂ O ₃	18.53 ± 0.16	19.62 ± 0.10	23.09 ± 0.09
K ₂ O	7.39 ± 0.08	8.61 ± 0.13	4.82 ± 0.07
Fe ₂ O ₃	6.71 ± 0.20	6.09 ± 0.16	13.31 ± 0.16
TiO ₂	1.10 ± 0.04	1.41 ± 0.03	1.22 ± 0.02
Na ₂ O	0.60 ± 0.06	0.34 ± 0.11	0.00 ± 0.00
P ₂ O ₅	0.30 ± 0.06	0.38 ± 0.06	0.00 ± 0.00
MnO	0.37 ± 0.01	0.77 ± 0.03	0.35 ± 0.01
MgO	0.28 ± 0.00	0.21 ± 0.02	0.59 ± 0.02
SO ₃	0.16 ± 0.01	0.20 ± 0.01	0.13 ± 0.01
V ₂ O ₅	0.06 ± 0.00	0.07 ± 0.00	0.09 ± 0.01
ZrO ₂	0.03 ± 0.00	0.04 ± 0.01	0.05 ± 0.00
ZnO	0.02 ± 0.00	0.02 ± 0.00	0.04 ± 0.00
Rb ₂ O	0.02 ± 0.00	0.02 ± 0.00	0.03 ± 0.00
SrO	0.01 ± 0.00	0.02 ± 0.00	0.01 ± 0.00
Ir ₂ O ₃	0.01 ± 0.00	0.01 ± 0.00	0.02 ± 0.00
Cr ₂ O ₃	0.01 ± 0.00	0.01 ± 0.00	0.00 ± 0.00
Y ₂ O ₃	0.00 ± 0.00	0.00 ± 0.00	0.00 ± 0.00
total	100.00	100.00	100.00

^aThe final ratios of samples were modified for total = 100.0%.

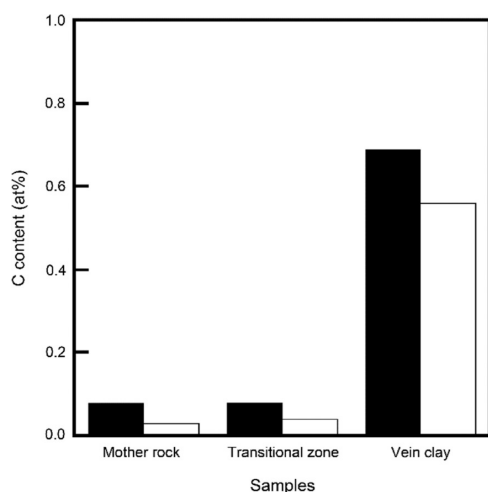


Figure 6. Total carbon (black bar) and organic carbon (white bar) content of rock core samples.

not always coincident with the shapes of voids of quartz. Noteworthy, the bright intensities of outer parts of luminescence domains were higher than those of inner parts.

The morphology and surface structure of quartz crystals were further evaluated. Most quartz crystals exhibited a smooth surface (Figure 7). Some of the obtained quartz crystals also exhibited typical skeleton-shaped crystals. Figure 8 shows the surface structures of typical skeleton-shaped crystals of quartz. Both {1–11} and {111} faces exhibited a typical center-recessed structure and developed a rim structure. The fine surface structures of the quartz crystals were observed by differential interference contrast (DIC) microscopy. The surface structure of the rim areas was essentially smooth; however, numerous small peaks and steps were also present. Furthermore, in the central part of the crystal surface, numerous steps of several μm in height were observed.

MicroCT analysis of the samples indicated the fine three-dimensional (3D) structure of samples. Figure 9 shows the

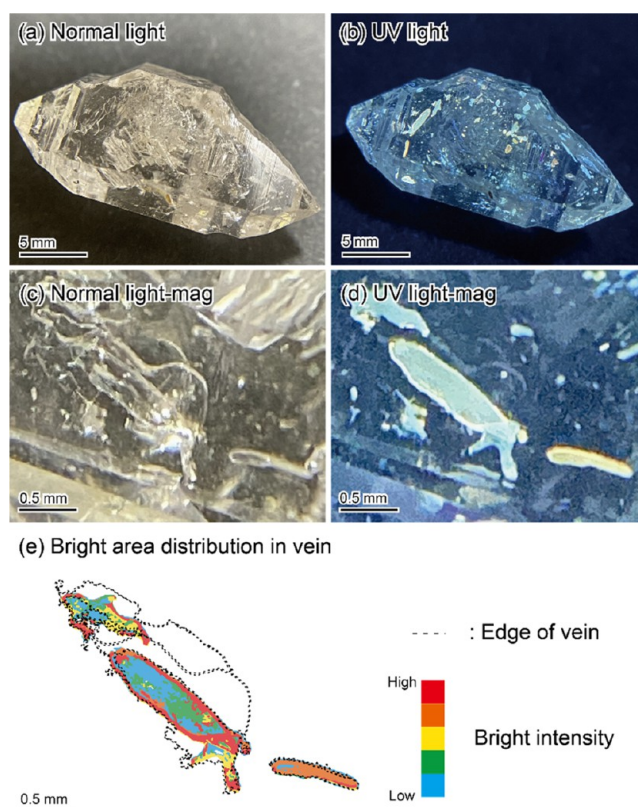


Figure 7. Photographs of representative oil–quartz crystals. (a) Normal light. (b) UV light. (c) Magnified image of the void under normal light. (d) Magnified image of the void under UV light. (e) Relationship of bright intensity of the luminescence area and void structure of (c).

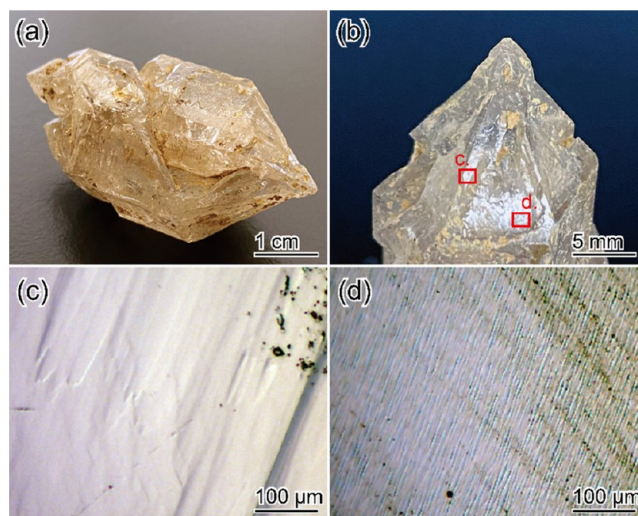


Figure 8. Photographs of representative oil–quartz skeleton crystals. (a) Whole image. (b) Magnified image of the top view. (c) DIC image of the rim structure of the skeleton crystal {1–11}. (d) DIC image of the center structure of the skeleton crystal {1–11}.

microCT images of representative oil–quartz crystals with photographs under normal and UV light. The 3D shapes of voids were located along the quartz {111} and {1–11} faces as bowl-type ones. The bottom of the void revealed a flat shape; on the other hand, the outer face of the void was curved. Combined with UV irradiation observation, luminescence

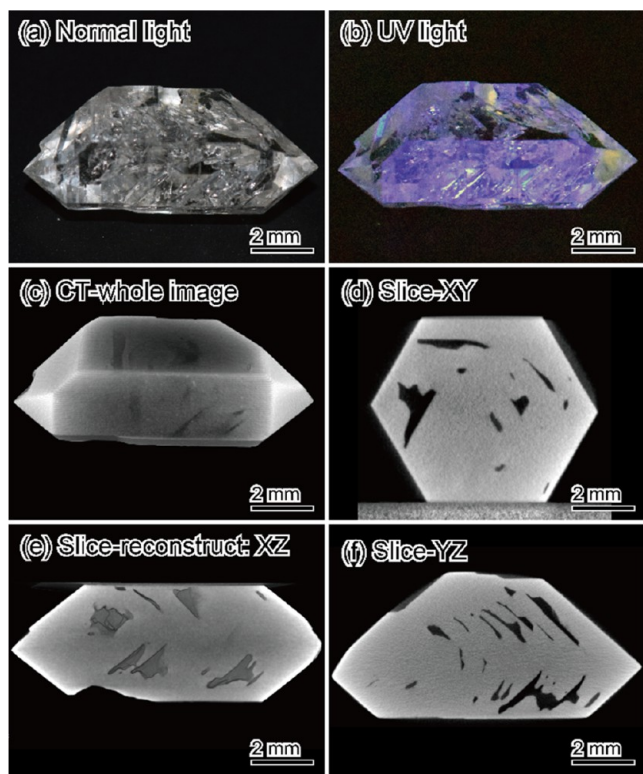


Figure 9. MicroCT image of the representative oil–quartz crystal. (a, b) Photograph of the oil–quartz crystal for facilitating comparison. (c) Reconstruct image of the whole structure. (d) XY-slice. (e) Reconstruct slice of XZ. (f) YZ-slice.

regions were located at the bottom and edge parts of void structures. In addition, some void structures were fused to each other. These void structures illustrate typical skeleton crystal structures, which are formed at a rapid growth rate. Thus, considering the morphology of oil–quartz, i.e., double-terminated and skeleton crystals, oil–quartz crystals were homogeneously nucleated in a growth field of clay veins.

The oil extracted from the voids of oil–quartz crystals was spectroscopically analyzed (Figure 10). In the UV region, two important irradiation bands were observed. Furthermore, in the visible region, two irradiation bands at 412 and 565 nm exhibited purple and green color luminescence, respectively.

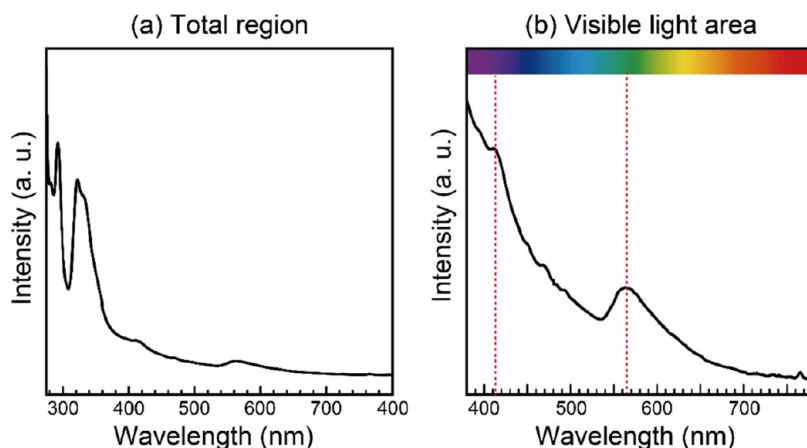


Figure 10. Fluorescence spectrum of the extracted oil sample from oil–quartz crystals. (a) Whole wavelength. (b) Visible region.

The CHN content of the extracted oil from oil crystals was 70.59, 11.25, and 1.07 atom %, respectively.

The oil samples were also extracted from rock core samples and oil–quartz crystals for estimating the origin of organic matters in oil–quartz crystals. Figure 11 shows the FTIR spectra of the extracted oil samples. All extracted oil samples revealed C–H, C–O, and C=O bonding of fatty acid and aromatic molecules along with the alkyl chain bonding (C–C). Furthermore, amido bonding was also slightly detected in the oil–quartz crystals.

Gas chromatography–mass spectrometry (GC–MS) analyses of the extracted oil samples were performed for identification of the composition of organic molecules. Figure 12 shows the GC–MS spectra of the extracted oil samples from oil–quartz crystals and rock core samples. Unlike the oil samples extracted from rock core samples, The oil–quartz crystals showed several bands and later retention times indicated various molecules. Figure 13 and Table 2 show the ratio of the C number and the molecular list of oil compositions, respectively. Except the transition zone, the rate of C14 molecules was relatively high in extracted oils from oil–quartz crystals and rock core samples. In the transition zone, although a similar tendency was revealed in thin-sectional observation, it was the tendency that the extracted oil consisted of low-molecular weight molecules. The main components of organic molecules in the parent rock core and clay vein were aromatic molecules and alkanes, such as 2,4-di-*tert*-butylphenol, 1,3-di-*tert*-butylbenzene, and tridecane. Furthermore, aromatic esters and butyl phthalate were detected. Alkanes and alcohol molecules were primarily detected in the transition zone.

In the case of oil–quartz crystals, although some of the detected molecules were the same as the cases of the parent rock core and clay vein parent, it was noteworthy that two C40 molecules were identified as terpene with fatty acid and low-molecular weight alcohol.

The detected terpene molecules were identified as lycopene and coleon F dimer. Noteworthy, lycopene and its derivatives exhibited fluorescence ability. Previous studies indicated that the irradiation band of lycopene was ~ 415 nm.^{28–30} Then, we could conclude that one of the true characters of luminescence in oil–quartz crystals was lycopene at the least lower wavelength irradiation. On the other hand, a luminescence band of lycopene hardly coincided the irradiation band of 560 nm and fluorescence abilities of the detected molecules in the

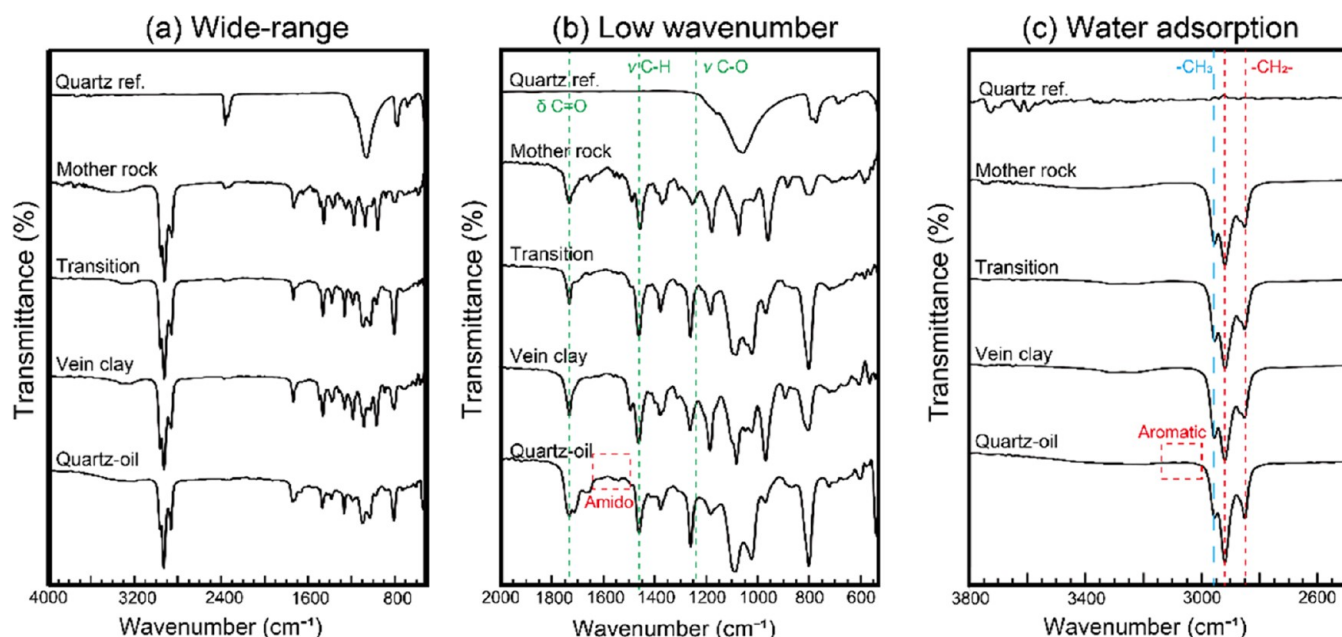


Figure 11. FT-IR spectra of extracted oil samples from the rock core and oil–quartz crystal samples. (a) Wide range. (b) Low wavenumber. (c) Water adsorption.

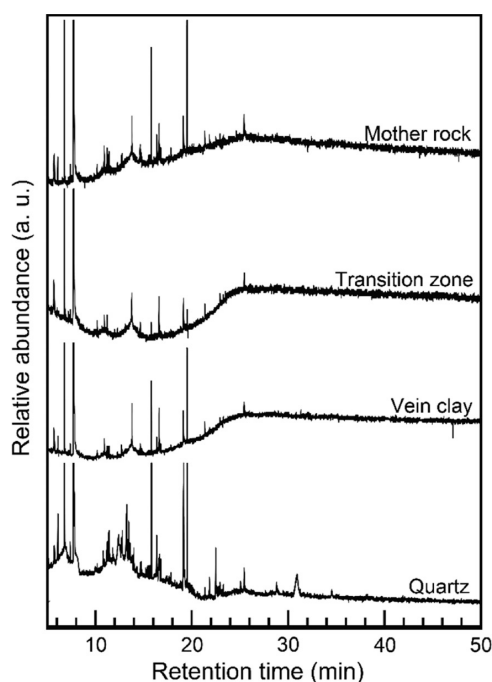


Figure 12. GC-MS spectra of the extracted oil samples from rock core and oil–quartz crystal samples.

extracted oil samples. However, some previous studies indicated that the metal complexes of some aromatic molecules exhibited fluorescence ability, for example, lanthanoids.^{31–33} Then, we considered that the irradiation band of 560 nm originated such aromatic molecules with metal complex forms.

The typical skeleton crystal shapes of oil–quartz crystals and domains of oils indicated that oil was included quickly during the growth process of quartz crystals,^{34,35} and the quick growth of quartz crystals with oils caused the formation of the shapes. XRD measurements indicated that the clay vein parent contained few amounts of feldspar, whereas a large amount

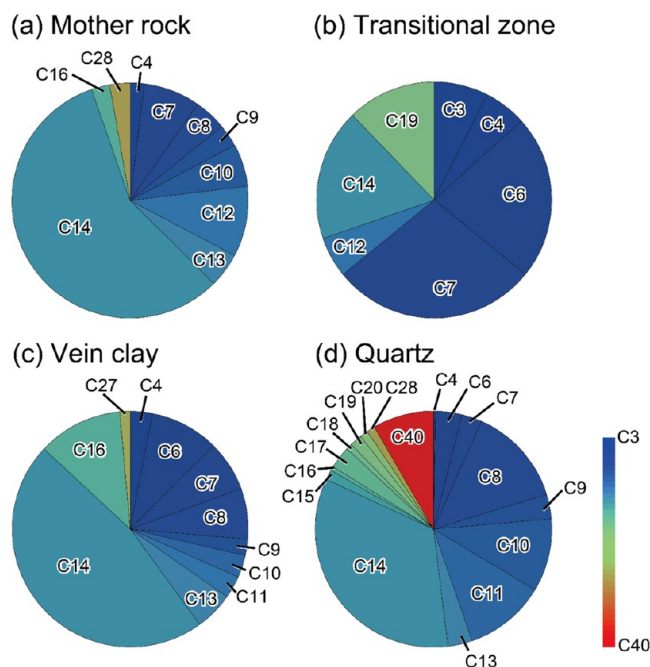


Figure 13. Existence ratios of each carbon number molecule in the extracted oil samples from rock core and oil–quartz crystals samples. (a) Mother rock. (b) Transitional zone. (c) Vein clay. (d) Quartz.

of feldspar was detected in the parent rock. Therefore, it was indicated that the feldspar decomposition process released the silica source for quick growth of quartz. Indeed, high temperature conditions (hydrothermal conditions) accelerated the decomposition process of feldspar and led to release of silica.^{36–38} However, organic molecules existing in oil–quartz crystals strongly regulated the upper temperature for growth fields. Considering the thermal stability of lycopene, the oil–quartz crystal formation reaction proceeded at ~ 80 °C.^{39–41}

The origin of oil in oil–quartz crystals was discussed. As shown in spectroscopic evaluations, the compositions of oil in

Table 2. List of Detected Organic Molecules in Extracted Oil Samples from the Rock Core and Oil–Quartz Crystals Samples

chemical name	chemical formula	C number	classification	fluorescence	mother rock	transitional zone	vein clay	quartz–oil
2,4-di- <i>tert</i> -butylphenol	C ₁₄ H ₂₂ O	14	aromatic		28.247		25.279	16.502
1,3-di- <i>tert</i> -butylbenzene	C ₁₄ H ₂₂	14	aromatic		17.532	8.491	17.472	10.530
<i>p</i> - <i>tert</i> -butylbenzoic acid	C ₁₁ H ₁₄ O ₂	11	aromatic					9.052
butyl phthalate	C ₁₆ H ₂₂ O ₄	16	aromatic ester				11.152	
Kesscoflex MCP	C ₁₄ H ₁₈ O ₆	14	aromatic ester			9.434		
tridecane	C ₁₃ H ₂₈	13	alkane		4.221		5.204	
trans-2,2,4,5-tetramethyl-1,3-dioxolane	C ₇ H ₁₄ O ₂	7	dioxolane		3.896	16.038	3.346	
lycopene	C ₄₀ H ₅₆	40	terpene	+				7.389
6-methyl-1-heptanol	C ₈ H ₁₈ O	8	alcohol					6.034
2-propyl-1-heptanol	C ₁₀ H ₂₂ O	10	alcohol					4.126
5-methyl-1-heptene	C ₈ H ₁₆	8	alkene					3.633
myristic acid	C ₁₄ H ₂₈ O ₂	14	fatty acid					3.510
3-methyl-5-undecene	C ₁₂ H ₂₄	12	alkene		9.091			
6-methyl-1-octene	C ₉ H ₁₈	9	alkene					2.278
4-methyl-pent-4-en-2-one	C ₆ H ₁₀ O	6	diene		3.247	13.208	3.717	
4-methylheptane	C ₈ H ₁₈	8	alkane		4.221			2.217
1,2-dimethylpropyl acetate	C ₇ H ₁₄ O ₂	7	ketone		3.247	12.264	3.346	
2,3,4-trimethylhexane	C ₉ H ₂₀	9	alkane		2.922			
1,2-diacetylene	C ₆ H ₈ O ₂	6	alkane		2.922	9.434		
2,3,4-trimethylpentane	C ₈ H ₁₈	8	alkane				4.461	
4,6-dimethyl-dodecane	C ₁₄ H ₃₀	14	alkane				2.974	
5-hydroxy-2,4-di- <i>tert</i> -butylphenyl-pentansaeure	C ₁₉ H ₃₀ O ₃	19	alcohol			12.264		
vinyl formate	C ₃ H ₄ O ₂	3	aldehyde			7.547		
chloro- <i>tert</i> -butanol	C ₄ H ₉ ClO	4	alcohol			5.660		
3,6-dimethyl-decane	C ₁₂ H ₂₆	12	alkane			5.660		
others					20.455		23.048	34.729
					100	100	100	100

oil–quartz crystals were different from those of rocks. The extracted oil from oil–quartz crystals contained terpene molecules (lycopene and coleon F), which were essential components of microorganism membranes.^{42,43} This observation suggested that the hydrothermal conditions, namely oil–quartz crystal formation field, might be also with bacterial coculture conditions and record the evidence of bacterial activity. Below 80 °C conditions, some thermophilic bacteria were likely to grow, such as *Thermotoga Sp.* and *Pyrodictiaceae Sp.*^{44–48} Thus, this foundation would introduce a novel interdisciplinary research field for geological events at lower temperature such as mineral formations affected by microorganisms.

3. CONCLUSIONS

We investigated the origin of oil–quartz crystals that exhibit fluorescence, obtained from Shimanto-cho, Kochi prefecture, Shikoku Island, Japan. The fluorescence domains in oil–quartz crystals were located at the voids of skeleton crystals. The origin of fluorescence was attributed to lycopene. Considering the thermal stability of lycopene and crystal morphology, oil–quartz crystals formed under extreme supersaturated conditions and low temperature (<80 °C).

4. EXPERIMENTAL METHODS

4.1. Reagents for Analysis. All reagents were purchased from FUJI Film Wako Pure Chemical Inc. Co., Japan, as reagent grade.

4.2. Preparation of Bulk Analysis Samples of Rock Core and Quartz Samples. The obtained rock core samples were trimmed off the outer weathered part; then, the treated

rock core samples and quartz samples were roughly crushed onto a steel anvil to prepare 1–2 cm-sized granules. The crushed granules were put into distilled water with a supersonic washing process three times. Then, the washed samples were dried in a dry oven at 40 °C for 2 d. The dried granules were well crushed using a preburned Al₂O₃ mortar and pestles. Then, the crushed powder of the samples was stored in PP vessels.

4.3. Extraction of Oil Samples from Rock Core and Quartz Samples. Approximately 1 g of the prepared powder samples was soaked into 10 mL of reagent-grade acetone and tightly sealed. Then, the sealed samples were gently shaken at 60 rpm in a shaking incubator at 40 °C for 12 h. After soaking, the treated skim of the samples was filtrated using a 220 nm syringe filter. Then, the filtered skim of the samples was put into a PP tube; then, vacuum conditions were used to vaporize acetone.

4.4. Characterization of Solid-State Materials. All samples and location photographs were obtained using a digital camera (XP140, FUJI Film Co., Japan) at effective pixels of 16 Mpixels.

The crystallographic details of the samples were obtained using XRD (MiniFlex600, Rigaku Co., Japan) at an acceleration voltage and amplitude of 40 kV and 15 mA, respectively. The diffraction angle was continuously scanned over $2\theta = 3\text{--}90^\circ$ at a scanning rate of $2^\circ/\text{min}$ for characterization.

The chemical bond structure of the samples was determined using Fourier transform infrared spectroscopy (FT-IR: IRTracer-100, Simadzu Co., Japan) equipped with a triglycine sulfate detector (20 scans, resolution 2 cm^{-1}) with an

attenuated total reflection diamond prism. All measurements were performed against an atmospheric background.

The atomic content of the samples was measured via energy-dispersive X-ray fluorescence spectroscopy (XRF: EDX-8100, Shimadzu Co., Japan) at an acceleration voltage of 15 kV under vacuum conditions.

The amount of CHN in the specimens was measured using carbon–hydrogen–nitrogen analysis (CHN-analysis: MT-6, Yanaco Co., Kyoto, Japan) using Ar gas as the carrier gas after drying in a P₂O₅ desiccator. For organic C contents of sample evaluation, 0.1 g of the crushed rock sample was immersed into 15 mL of 25 wt % NaClO solution for 1 day at R.T. Then, the treated samples were washed with distilled water several times and eventually dried.

The fine structure of the samples was observed using field emission scanning electron microscopy (FE–SEM: JSM-6700F, JEOL Co., Japan) at an acceleration voltage of 3 kV after Os sputtering.

The 3D image of the samples was measured using a quantitative three-dimensional evaluation program, which is included in the microcomputed tomography system (microCT: ScanXmate-L080T, Comscantecno Co., Japan) with a source voltage (69 kV) and source current (149 μA) with an Al filter (0.5 mm). The voxel resolution was 125 μm³.

Gas chromatography–mass spectrometry (GC–MS) analyses were performed with a GCMS-QP2010 (Shimadzu Co., Japan) gas chromatograph magnetic sector mass spectrometer using He gas as a carrier gas with a constant flow of 1 mL/min. An Agilent J&W DB-5 (Agilent Technology Japan, Japan) capillary column (0.25 mm i.e., film thickness of 1.00 μm) with a 30 m-long integrated guard column was used. The GC oven was programmed for an initial temperature of 50 °C for 3 min, followed by heating at 10 °C/min to 250 °C with 37 min final hold time.

The fluorescence spectra of the samples were measured using a spectrofluorometer (FP-8550: JASCO Co., Japan) using irradiation wavelength at 265 nm and the measurement wavelength range from 275 to 850 nm at a scanning rate of 200 nm/min. Oil samples were coated onto the quartz glass for measurement.

AUTHOR INFORMATION

Corresponding Author

Yuki Sugiura – Health and Medical Research Institute, National Institute of Advanced Industrial Science and Technology (AIST), Takamatsu 761-3095 Kagawa, Japan; Research Planning Office, Headquarters of Department of Life Science and Biotechnology, National Institute of Advanced Industrial Science and Technology (AIST), Tsukuba 305-0035 Ibaraki, Japan; orcid.org/0000-0003-1472-5435; Email: yuki-sugiura@aist.go.jp

Authors

Naoko Tobita – Friends of Mineral, Tokyo 176-0013, Japan
Takashi Tobita – Friends of Mineral, Tokyo 176-0013, Japan
Masaru Taga – Faculty of Agriculture, Ryukoku University, Ohtsu, Shiga, Japan 520-2194
Shu Nakachi – Natural History Lab., Kochi 788-0313, Japan
Kazumichi Yokota – Health and Medical Research Institute, National Institute of Advanced Industrial Science and Technology (AIST), Takamatsu 761-3095 Kagawa, Japan; orcid.org/0000-0002-8590-2737

Etsuko Yamada – Health and Medical Research Institute, National Institute of Advanced Industrial Science and Technology (AIST), Takamatsu 761-3095 Kagawa, Japan
Masanori Horie – Health and Medical Research Institute, National Institute of Advanced Industrial Science and Technology (AIST), Takamatsu 761-3095 Kagawa, Japan
Koichi Momma – Department of Geology and Paleontology, National Museum of Nature and Science, Tsukuba 305-0005 Ibaraki, Japan
Satoshi Matsubara – Department of Geology and Paleontology, National Museum of Nature and Science, Tsukuba 305-0005 Ibaraki, Japan

Complete contact information is available at:
<https://pubs.acs.org/10.1021/acsomega.3c00272>

Notes

The authors declare no competing financial interest.

ACKNOWLEDGMENTS

The authors thank Dr. M. Kawasaki and A. Tokumoto for scientific discussions. The authors thank T. Baba (JASCO Co.) for fluorescence spectrometry measurements and Prof. H. Terasaki (Okayama Univ.) for microscopy observation. The authors thank Drs. Y. Suezawa, T. Nakanishi, and S. Asahi (RIST Kagawa) for helping with FT-IR and GC-MS measurements. This study was partially supported by the Research Center for Industrial Science & Technology, Kagawa Industry Support Foundation (RIST Kagawa). This study was financially supported by the Kazuchika Okura Memorial Foundation and JST Core Research for Evolutionary Science and Technology (JST-CREST), Grant number: JPMJCR22L5.

REFERENCES

- (1) Pearson, D. G.; Brenker, F. E.; Nestola, F.; McNeill, J.; Nasdala, L.; Hutchison, M. T.; Matveev, S.; Mather, K.; Silversmit, G.; Schmitz, S.; Vekemans, B.; Vincze, L. Hydrous mantle transition zone indicated by ringwoodite included within diamond. *Nature* **2014**, *507*, 221–229.
- (2) Frezzotti, M. L.; Tecce, F.; Casagli, A. Raman spectroscopy for fluid inclusion analysis. *J. Geochem. Explor.* **2012**, *112*, 1–20.
- (3) Sobolev, N. V.; Kaminsky, F. V.; Griffin, W. L.; Yefimova, E. S.; Win, T. T.; Ryan, C. G.; Botkunov, A. I. Mineral inclusions in diamonds from the Sputnik kimberlite pipe, Yakutia. *Lithos* **1997**, *39*, 135–157.
- (4) Promwongnan, S.; Sutthirath, C. Mineral Inclusions in Ruby and Sapphire from the Bo Welu gem Deposit in Chanthaburi, Thailand. *Gem Gemol.* **2019**, *55*, 354–369.
- (5) Bui, T. N.; Entremont, P.; Gauthier, J.-P. Large 12-Rayed Black Star Sapphire from Sri Lanka with Asterism Caused by Ilmenite Inclusions. *J. Gemmol.* **2017**, *35*, 430–435.
- (6) Farfan, G. A.; Post, J. E. Quartz from Madagascar with Fuchsite Phantom Inclusions. *J. Gemmol.* **2019**, *36*, 698–699.
- (7) Gurov, V. V.; Tsvetkov, E. G.; Kiryashkin, A. G. Features of beryllium aluminate crystal growth by the method of horizontally oriented crystallization. *J. Cryst. Growth* **2003**, *256*, 361–367.
- (8) VanSpeybroeck, V.; Hemelsoet, K.; Joos, L.; Waroquier, M.; Bell, R. G.; Catlow, C. R. A. Advances in theory and their application within the field of zeolite chemistry. *Chem. Soc. Rev.* **2015**, *44*, 7044–7111.
- (9) Zhang, R.; Liu, N.; Lei, Z.; Chen, B. Selective Transformation of Various Nitrogen-Containing Exhaust Gases toward N₂ over Zeolite Catalysts. *Chem. Rev.* **2016**, *116*, 3658–3721.
- (10) Ye, Q.; Zhou, F.; Liu, W. Bioinspired catecholic chemistry for surface modification. *Chem. Soc. Rev.* **2011**, *40*, 4244–4258.

- (11) Mousa, M.; Evans, N. D.; Oreffo, R. O. C.; Dawson, J. I. Clay nanoparticles for regenerative medicine and biomaterial design: A review of clay bioactivity. *Biomaterials* **2018**, *159*, 204–214.
- (12) Nakamura, R.; Takashima, T.; Kato, S.; Takai, K.; Yamamoto, M.; Hashimoto, K. Electrical Current Generation across a Black Smoker Chimney. *Angew. Chem., Int. Ed.* **2010**, *49*, 7692–7694.
- (13) Furukawa, Y.; Sekine, T.; Oba, M.; Kakegawa, T.; Nakazawa, H. Biomolecule formation by oceanic impacts on early Earth. *Nat. Geosci.* **2009**, *2*, 62–66.
- (14) Kim, H. J.; Furukawa, Y.; Kakegawa, T.; Bitá, A.; Scorei, R.; Benner, S. A. Evaporite borate-containing mineral ensembles make phosphate available and regiospecifically phosphorylate ribonucleosides: borate as a multifaceted problem solver in prebiotic chemistry. *Angew. Chem., Int. Ed.* **2016**, *55*, 15816–15820.
- (15) Momma, K.; Ikeda, T.; Nishikubo, K.; Takahashi, N.; Honma, C.; Takada, M.; Furukawa, Y.; Nagase, T.; Kudoh, Y. New silica clathrate minerals that are isostructural with natural gas hydrates. *Nat. Commun.* **2011**, *2*, 196–202.
- (16) Nakamura, T.; Matsumoto, M.; Amano, K.; Enokido, Y.; et al. Formation and evolution of carbonaceous asteroid Ryugu: Direct evidence from returned samples. *Science* **2022**, *379*, No. eabn8671.
- (17) Parnell, J.; Carey, P. F.; Monson, B. Fluid inclusion constraints on temperatures of petroleum migration from authigenic quartz in bitumen veins. *Chem. Geol.* **1996**, *129*, 217–226.
- (18) Munz, I. A.; Yardley, B. W. D.; Banks, D. A.; Wayne, D. Deep penetration of sedimentary fluids in basement rocks from southern Norway: Evidence from hydrocarbon and brine inclusions in quartz veins. *Geochim. Cosmochim. Acta* **1995**, *59*, 239–254.
- (19) Feely, M.; Costanzo, A.; Lindner, F.; George, J.; Parnell, J.; Bowden, S.; Baba, M.; Owens, P. Quartz-Amethyst Hosted Hydrocarbon-Bearing Fluid Inclusions from the Green Ridge Breccia in the Snoqualmie Granite, North Cascades, WA, USA. *Minerals* **2017**, *7*, No. 174.
- (20) George, S. C.; Volk, H.; Dutkiewicz, A.; Ridley, J.; Buick, R. Preservation of hydrocarbons and biomarkers in oil trapped inside fluid inclusions for >2 billion years. *Geochim. Cosmochim. Acta* **2008**, *72*, 844–870.
- (21) Suchý, V.; Dobes, P.; Sykorova, I.; Machovic, V.; Stejskal, M.; Kroufek, J.; Chudoba, J.; Matejovsky, L.; Havelcova, M.; Matysova, P. Oil-bearing inclusions in vein quartz and calcite and, bitumens in veins: Testament to multiple phases of hydrocarbon migration in the Barrandian basin (lower Palaeozoic), Czech Republic. *Mar. Pet. Geol.* **2010**, *27*, 285–297.
- (22) Katto, J. Sedimentary structures from the Shimanto Terrain, Shikoku, Southwest Japan. *Res. Rep. Kochi Univ.* **1961**, *13*, 45–58.
- (23) Geological map: Kubokawa, Kanehara, N. eds., *Imperial Geological Survey of Japan*, 1933.
- (24) Taira, A. Sedimentary evolution of Shikoku subduction zone: The Shimanto Belt and Nankai Trough. In *Formation of Active Ocean Margins*; Nasu, N.; Kobayashi, K.; Uyeda, S.; Kushiro, I.; Kagami, H., Eds.; Terrapub, 1985; pp 835–851.
- (25) Yanai, S. Megakink bands and Miocene regional stress field in Outer Southwest Japan. *Sci. Pap. Coll. Arts. Sci. Univ. Tokyo* **1986**, *36*, 55–79.
- (26) Kiminami, K.; Oyaizu, A.; Ishihama, S.; Miura, K. Chemical composition of sandstones from the Cretaceous Shimanto Belt, western Shikoku, Japan, and correlation of petrofacies units in the Northern Shimanto Belt. *Mem. Geol. Soc. Jpn.* **2000**, *57*, 107–117.
- (27) Oyaizu, A.; Miura, K.; Tanaka, T.; Hayashi, H.; Kiminami, K. Geology and radiolarian ages of the Shimanto Supergroup, western Shikoku, Southwest Japan. *J. Geol. Soc. Jpn.* **2002**, *108*, 701–720.
- (28) Alwis, D. D. D. H.; Chandrika, U. G.; Jayaweera, P. M. Spectroscopic studies of neutral and chemically oxidized species of β -carotene, lycopene and norbixin in CH₂Cl₂: Fluorescence from intermediate compounds. *J. Lumin.* **2015**, *158*, 60–64.
- (29) Numan, N.; Jeyaram, S.; Kaviyarasu, K.; Neethling, P.; Sackey, J.; Kotsedi, C. L.; Akbari, M.; Morad, R.; Mthunzi-Kufa, P.; Sahraoui, B.; Maaza, M. On the remarkable nonlinear optical properties of natural tomato lycopene. *Sci. Rep.* **2022**, *12*, No. 9078.
- (30) Fujii, R.; Onaka, K.; Nagae, H.; Koyama, Y.; Watanabe, Y. Fluorescence spectroscopy of all-trans-lycopene: comparison of the energy and the potential displacements of its 2Ag⁻ state with those of neurosporene and spheroidene. *J. Lumin.* **2001**, *92*, 213–222.
- (31) Tian, D.; Li, Y.; Chen, R.-Y.; Chang, Z.; Wang, G.-Y.; Bu, X.-H. A luminescent metal–organic framework demonstrating ideal detection ability for nitroaromatic explosives. *J. Mater. Chem. A* **2014**, *2*, 1465–1470.
- (32) Bradbury, A. J.; Lincoln, S. F.; Wainwright, K. P. Fluorescence signaling of aromatic oxoanion inclusion within metal-ion activated molecular receptor complexes formed from 2-(9-anthracenylmethylamino)ethyl-appended cyclen. *J. Inclusion Phenom. Macrocyclic Chem.* **2011**, *71*, 567–575.
- (33) Marmodée, B.; de Klerk, J. S.; Ariese, F.; Gooijer, C.; Kumke, M. U. High-resolution steady-state and time-resolved luminescence studies on the complexes of Eu(III) with aromatic or aliphatic carboxylic acids. *Anal. Chem. Acta* **2009**, *652*, 285–294.
- (34) Barbee, O.; Chesner, C.; Deering, C. Quartz crystals in Toba rhyolites show textures symptomatic of rapid crystallization. *Am. Mineral.* **2020**, *105*, 194–226.
- (35) Sunagawa, I. *Crystals Growth, Morphology and Perfection*, Cambridge University Press: U.K., 2005.
- (36) Su, S.; Ma, H.; Chuan, X. Hydrothermal decomposition of K-feldspar in KOH–NaOH–H₂O medium. *Hydrometallurgy* **2015**, *156*, 47–52.
- (37) Schepers, A.; Milsch, H. Dissolution–precipitation reactions in hydrothermal experiments with quartz–feldspar aggregates. *Contrib. Mineral. Petrol.* **2013**, *165*, 83–101.
- (38) Wild, B.; Daval, D.; Guyot, F.; Knauss, K. G.; Pollet-Villard, M.; Imfeld, G. pH-dependent control of feldspar dissolution rate by altered surface layers. *Chem. Geol.* **2016**, *442*, 148–159.
- (39) Hackett, M. M.; Lee, J. H.; Francis, D.; Schwartz, S. J. Thermal Stability and Isomerization of Lycopene in Tomato Oleoresins from Different Varieties. *J. Food Sci.* **2006**, *69*, 536–541.
- (40) Qiu, W.; Jiang, H.; Wang, H.; Gao, Y. Effect of high hydrostatic pressure on lycopene stability. *Food Chem.* **2006**, *97*, 516–523.
- (41) Chen, J.; Shi, J.; Xue, S. J.; Ma, Y. Comparison of lycopene stability in water- and oil-based food model systems under thermal- and light-irradiation treatments. *LWT – Food Sci. Technol.* **2009**, *42*, 740–747.
- (42) Hayakawa, H.; Motoyama, K.; Sobue, F.; Hemmi, H.; et al. Modified mevalonate pathway of the archaeon *Aeropyrum pernix* proceeds via trans-anhydromevalonate 5-phosphate. *Proc. Natl. Acad. Sci. U.S.A.* **2018**, *115*, 10034–10039.
- (43) Umeno, D.; Tobias, A. V.; Arnold, F. H. Evolution of the C30 Carotenoid Synthase CrtM for Function in a C40 Pathway. *J. Bacteriol.* **2002**, *184*, 6690–6699.
- (44) Kashefi, K.; Lovely, D. R. Extending the Upper Temperature Limit for Life. *Science* **2003**, *301*, No. 934.
- (45) Brock, T. D.; Freeze, H. *Thermus aquaticus* gen. n. and sp. n., a Nonsporulating Extreme Thermophile. *J. Bacteriol.* **1969**, *98*, 289–297.
- (46) Stetter, K. O. Ultrathin mycelia-forming organisms from submarine volcanic areas having an optimum growth temperature of 105 °C. *Nature* **1982**, *300*, 258–260.
- (47) Stetter, K. O.; König, H.; Stackebrandt, E. *Pyrodictium* gen. nov., a new genus of submarine disc-shaped sulphur reducing archaeobacteria growing optimally at 105 °C. *Syst. Appl. Microbiol.* **1983**, *4*, 535–551.
- (48) Huber, R.; Langworthy, T. A.; König, H.; Thomm, M.; Woese, C. R.; Sleytr, U. B.; Stetter, K. O. *Thermotoga maritima* sp. nov. represents a new genus of unique extremely thermophilic eubacteria growing up to 90 °C. *Arch. Microbiol.* **1986**, *144*, 324–333.
- (49) Levien, L.; Prewitt, C. T.; Weidner, D. J. Structure and elastic properties of quartz at pressure P = 1 atm. *Am. Mineral.* **1980**, *65*, 920–930.
- (50) Grundy, H. D.; Ito, J. The refinement of the crystal structure of a synthetic non-stoichiometric Sr feldspar. *Am. Mineral.* **1974**, *59*, 1319–1326.

(51) Viani, A.; Gualtieri, A.; Artioli, G. The nature of disorder in montmorillonite by simulation of X-ray powder patterns. *Am. Mineral.* **2002**, *87*, 966–975.